Wettability-Assisted Process to Shape Organic Crystalline Printed Films

ADVANCED MATERIALS INTERFACES
www.advmatinterfaces.de

Wettability-Assisted Process to Shape Organic Crystalline Printed Films

Sara Sequeira, Verónica Martins, Rui Vilarinho, Susana Cardoso, Joaquim A. Moreira, Helena Alves,* and Diana C. Leitao*

The controlled growth of organic crystalline materials in predefined locations still poses a challenge for functional device application such as phototransistors, photoconductors, or photovoltaic solar cells. This work evidences the use of optical lithography and a fluoroalkylsilane to selectively modify the surface energy and how to create a wettability micro-patterned structure. These are then combined with non-contact printing of the organic solution providing custom-shaped films. To deliver printed films with improved morphological quality, key process parameters for high-performance organic materials are optimized. Particular attention is given to the adjustment of the concentration and solvent mixture to tune the jetting properties, and consequently, slow down the evaporation rate. Continuous films are obtained for an optimized number of droplets and spacing between them. Micro-Raman spectroscopy imaging confirms the crystalline nature of the printed films and the lack of impurities. To validate the method, rubrene and triisopropylsilylethynyl (TIPS)-pentacene are tested using two-terminal optoelectronic devices. TIPS-pentacene rectangular printed micrometric photosensor presents linear behavior and no hysteresis, reaching 0.33 nA under 18.1 mW cm^{-2}. The structural and optoelectronic characterization is in line with other micro-patterned examples, opening doors for new industrial applications.

1. Introduction

The possibility of non-expensive and easy fabrication, combined with the capabilities to control the optical characteristics,[1] are the main advantages of organic photonic devices such as photodiodes,[2,3] phototransistors,[4,5] or resistive memories.[6,7] These issues are of fundamental interest, as future internet of things in infrastructures, transports, or wearables, will require a substantial number of optical sensors.[8,9] In particular, the ease of fabrication of the active parts of these devices following solution-processing routes, such as inkjet printing, can deliver polycrystalline smooth films, with precise control over the dispensed volume.[10] Critical aspects in developing a printable device include the quality of the materials, the solution formulation, viscosity control, surface wetting to avoid solution dispersion, or long-term stability.[11,12] Specifically, viscosity is not only important for the film quality but also determines the printing technique[13] and can be divided into two main types, low viscosity or high viscosity solutions. Typically, volatile solutions do not use binders, surfactants, or other chemical additives and offer higher-purity materials.[14] However, these can affect film morphology and topography, creating the well-known "coffee-ring" effect.[15] It also presents an increased spread area with limited control of defined structures and has difficulties in controlling crystal nucleation and molecular aggregation, leading to defects, uneven thickness, and inferior device performance.[16] In this case, large and aligned crystalline domains are highly important, as they offer low charge transport anisotropy and low density of grain boundaries leading to higher optical-to-electrical conversion.[17,18] Strategies using solution-processing techniques have enabled high crystallinity organic semiconductor films.[19] However, these approaches present little or even no control on both the shape and size of the active semiconductor

S. Sequeira, V. Martins, S. Cardoso, D. C. Leitao
Instituto de Engenharia de Sistemas e Computadores – Microsistemas e Nanotecnologias
Rua Alves Redol 9, Lisboa 1000-029, Portugal
E-mail: ssequeira@inesc-mn.pt

S. Sequeira, S. Cardoso
Instituto Superior Técnico
Universidade de Lisboa
Av. Rovisco Pais, Lisboa 1000-029, Portugal

The ORCID identification number(s) for the author(s) of this article can be found under https://doi.org/10.1002/admi.202200616.

DOI: 10.1002/admi.202200616

S. Sequeira, H. Alves
CICECO
Universidade de Aveiro
Campus de Santiago, Aveiro 3810-183, Portugal
E-mail: alves.helena@ua.pt

R. Vilarinho, J. A. Moreira
Departamento de Física e Astronomia
Instituto de Física de Materiais Avançados
Nanotecnologia e Fotónica
Faculdade de Ciências da Universidade do Porto
Rua do Campo Alegre s/n, Porto 4169-007, Portugal

D. C. Leitao
Department of Applied Physics
Eindhoven University of Technology
P.O. Box 513, Eindhoven 5600 MB, The Netherlands

layer. As most organic semiconductors are not compatible with conventional lithography and etching processes, this hinders the establishment of well-defined structures. This is especially important for optical resonators, where it is crucial to maintain device-to-device properties.[20] Attempts using chemical confinement onto interdigitated electrodes revealed the formation of single crystals even on highly heterogeneous surfaces, with good electrical contact.[21] However, the crystal distribution is random, forming irregular shapes. By merging inkjet printing with antisolvent crystallization, uniform films can be achieved and patterned crystalline films attained through controlled hydrophilic/hydrophobic regions.[22] Yet, this is achieved by a lengthy multistep process, and limited to surfaces with silanol groups with considered limitations in the substrate, device architecture, and layout.

Herein, a combination of drop-on-demand printing, a non-contact printing that enables smaller drop size and higher placement accuracy, and surface energy engineering is employed to print and grow tailored organic crystalline semiconductors in targeted locations with control over their optical and structural properties. The method is validated by fabricating a two-terminal photoconductor. The strategy here described opens up the possibility of manufacturing high-density arrays of micrometric or millimetric organic devices guaranteeing controlled size and shape, versatility, efficiency, and reproducibility.

2. Results and Discussion

2.1. Chemical Modification of Wettable Substrates

Surface wetting in hydroxylated surfaces, such as silica or alumina, typically hydrophilic, can be chemically modified through the assembling of organosilane layers. To significantly lower surface energy, fluoroalkylsilanes are more suitable than alkylsilanes, due to their highly hydrophobic tail.[23,24] The reactivity with hydroxylated surfaces depends on the anchoring groups of self-assembled monolayers (SAMs).[25] Although ethoxysilanes present slower reactivity, they originate nontoxic by-products upon silanization.[26] 1H,1H,2H,2H-Perfluorodecyltriethoxysilane (FDTES) presents all the aforementioned advantages, and in addition, it is not prone to chemical degradation below 350 °C.[27]

To assess the surface wetting behavior of FDTES on silica, contact angle measurements were performed. **Figure 1** compares the wettability of deionized (DI) water and toluene on as-deposited silica film (Figure 1a) and FDTES assembled on silica (Figure 1b). In the case of the untreated surface, the contact angles of the droplets are around 49° and less than 5° for water and toluene, respectively. As a result, a high-wettability organic solution that uses toluene or a mixture of chloroform, both common solvents used in organic semiconductors, will spontaneously spread on the substrate surface, due to the omniphilic character of the silica surface. Alternatively, when the surface is exposed to FDTES (molecular structure in Figure 1c, for at least 24 h under vacuum, a clear change in its wettability is observed. This fluoroalkylsilane compound reacts with the hydroxyl groups of the silica film, increasing water and toluene contact angles to around 89° and 35°, respectively (Figure 1b). These results are in line with the low-wettability of organic solvents in fluoroalkylsilanes coated surfaces when compared with alkylsilane SAMs.[23,28,29]

2.2. The Wettability-Assisted Printing Process

Making use of the low wetting behavior of a surface modified with FDTES, a protocol was developed to chemically confine a photoactive solution to wettable regions. Figure 1d outlines the implemented protocol. It comprises local modification of the silica wettability with FDTES and non-contact printing of the organic solution. Here, photolithography is used to define the size and shape of the SiO_2 regions protected by photoresist (PR) from the exposure to FDTES (step 3). After silanization and PR removal, a wettability-patterned substrate is engineered (step 4). The droplets of the solution containing the photoactive material are then dispensed via non-contact printing on the predefined wettable sites (hydrophilic region) and confined by the surrounding hydrophobic region to the area of interest (step 5). The non-contact printer is equipped with a piezoelectric activated tip that guarantees a drop-on-demand process. To demonstrate the method, two photosensitive organic materials were tested, namely rubrene (Figure 1e) and triisopropylsilylethynyl (TIPS)-pentacene (Figure 1f).

2.3. Printing Continuous-Shaped Films

Following the fabrication of the wettability-patterned substrate, the printing parameters were adjusted for the two organic materials used in this work, which could also be extendable to other printable materials. The optimization of the printing solution and the correlation between the wettable area and dispensing layout for complete coverage of the wettable area have been taken into account. Such an approach targets continuous and reproducible films with diminished structural defects (e.g., grain boundaries). This will reduce the charge transport anisotropy and trapping phenomena, leading to devices with faster response times, lower dark currents, and higher photocurrents.

The optimization of the printing solution comprises the selection of the organic solvent or mixture of solvents and tuning of the concentration of the photoactive material prior to focusing on the uniformity of the printed films.[30] The solvent choice takes into account three criteria: i) the solubility of the semiconductor material on the organic solvent based on the calculated Hansen sphere,[31] ii) its boiling point (single or binary mixture of organic solvents), and iii) vapor pressure. For proper jetting, the boiling point and the vapor pressure should be in the range of 100–210 °C and 0.2–50 mbar, respectively.[32] The concentration of the solution was altered to maximize solubility and avoid tip clogging during dispensing. To slow down the evaporation rate of the dispensed solution, the substrate was placed on a cooled stage (below 20 °C).[21] The applied piezoelectric voltage (V) was also adjusted between 50 and 80 V, according to the organic solution characteristics aiming to reduce the formation of secondary droplets.

The two chosen materials, rubrene and TIPS-pentacene, present very distinct solubility. Rubrene is insoluble in most low-toxicity organic solvents.[33,34] Thus, to print the rubrene films,

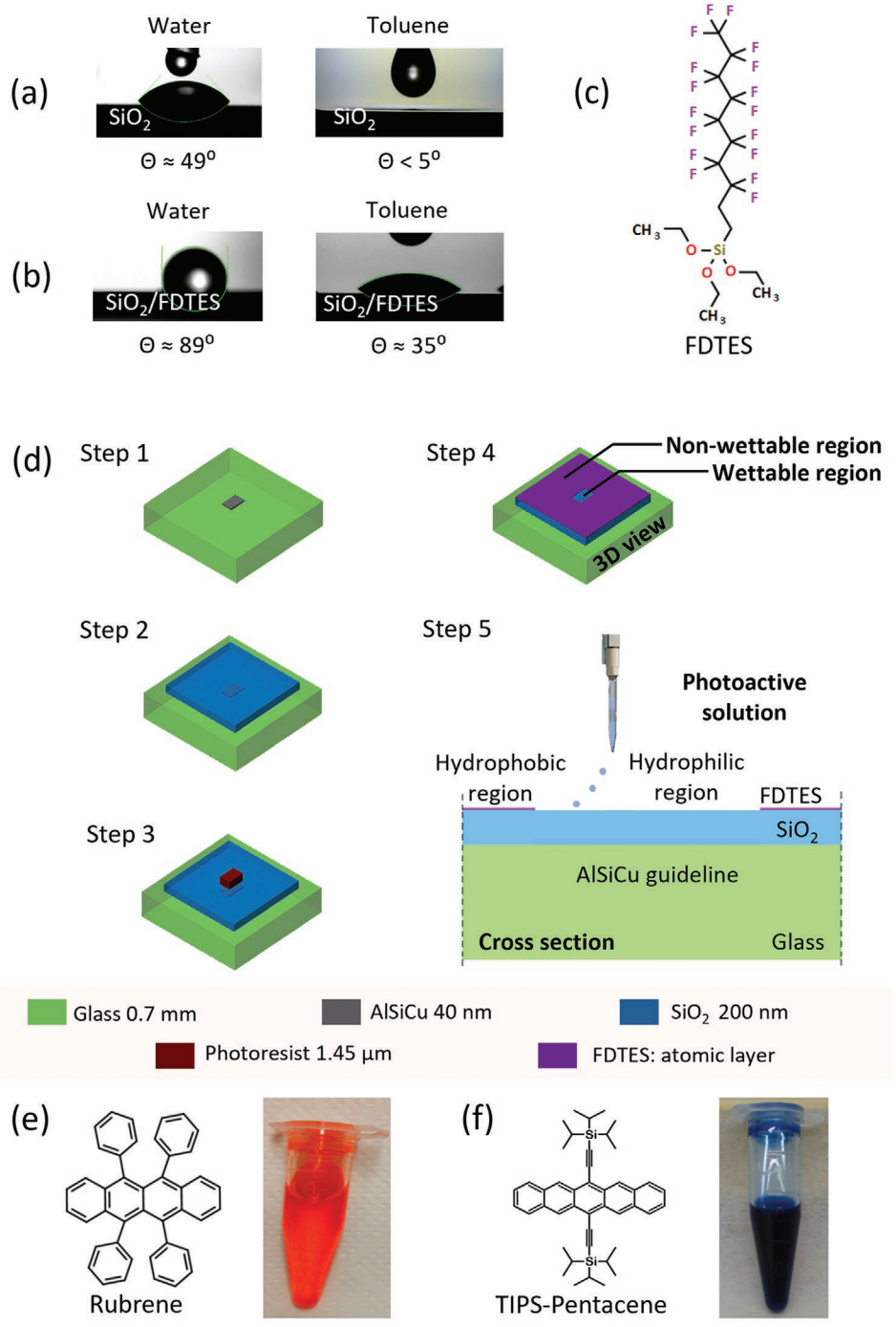

Figure 1. Deionized water and toluene contact angles on a) SiO_2 and b) SiO_2 coated with FDTES. c) Molecular structure of FDTES. d) Wettability-assisted process to define the photoactive printed region: Step 1 – AlSiCu markers definition, Step 2 – SiO_2 deposition, Step 3 – Photolithography, Step 4 –Wettability-patterned substrate, and Step 5 – Non-contact printing of the photoactive material. e) Molecular structure and rubrene dissolved in chloroform and toluene (10 mg mL^{-1}) (1:5 v/v) and f) Molecular structure and TIPS-pentacene dissolved in toluene (14.7 mg mL^{-1}).

a mixture of chloroform and toluene (1:5) (v/v) was used to dissolve 10 mg of rubrene powder. Toluene is the main solvent of the mixture due to its high boiling point and chloroform is necessary to increase the solubility of rubrene. An adequate proportion of the solvents is critical, as rubrene particles precipitation occurs if a lower ratio of chloroform is used, while for a higher ratio, the jetting becomes unstable. For this solution and printing system, the optimum stage temperature was found at 14 °C with a driving voltage of 60 V.

The number of droplets per spot and the spacing between spots (**Figure 2**a) were adjusted until the pre-defined wettable geometries were uniformly filled. By doing so, individual

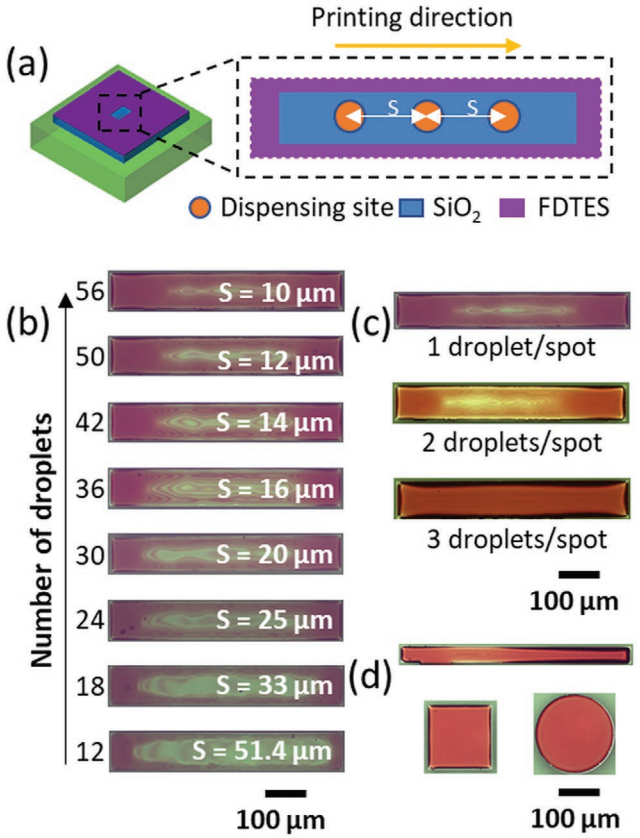

Figure 2. a) Representation of three dispensing sites and the spacing (*S*) between them on a rectangular wettable region. Effect of b) the number of droplets and spacing between droplets, c) the number of droplets per spot on the uniformity of a rectangular film (100×625 µm^2). d) Circular, quadrangular, and rectangular rubrene printed films of equivalent area (31 250 µm^2) printed with 42 droplets.

droplets coalesce to form a continuous film. In rectangular geometries, the droplets are dispensed in line, while in quadrangular and circular geometries, the equivalent number of droplets are dispensed in the same dispensing site at the center of the structure.

Figure 2b and c highlights the effect of the spacing (*S*) between dispensing sites and the number of droplets per spot on a rubrene printed film with a rectangular confinement area of 100×625 µm^2. Based on visual inspection, the uniformity of the film improves with decreasing spacing between spots and an increasing number of droplets per spot.[12] For this geometry, an optimal combination of three droplets per spot dispensed with 14 µm-spacing leads to a continuous film. The estimated droplet volume is around 172 pL, corresponding to a total dispensed volume of 21.7 nL.

Figure 2d shows circular (φ = 199 µm) and quadrangular (177×177 µm^2) printed films, equivalent in area to a rectangular feature (50×625 µm^2). The target geometries were fulfilled using a total of 42 droplets. Regardless of the shape and dimensions of the wettable region, the solution was well confined to the target region. Although, sometimes the formation of secondary droplets can alter the total dispensed volume and when these droplets deviate from the main droplet, some irregularities in the geometry of the printed films can be obtained. The darker contour observed at the border of the films is attributed to the coffee-ring effect. This is associated with the evaporation rate of the solvent being higher at the periphery than at the center of the wettable region.[35]

Due to the TIPS groups, TIPS-pentacene is much more soluble in a variety of solvents. The solubility of TIPS-pentacene increases in the following order: dimethylformamide (DMF), n-hexane, toluene, and chloroform.[31] To infer the effect of different solutions on the morphology of TIPS-pentacene printed films, several co-solvent combinations using these solvents were tested, setting the stage temperature to 14 °C. Both chloroform and n-hexane have boiling points around 60 °C,[36] while the boiling point of toluene and DMF is above 110 °C.[37,38] The solvent system of an orthogonal solvent (DMF) with a non-orthogonal solvent (toluene) induces rapid solute precipitation in regions with high surface energy.[35] The imbalance between nucleation and crystal growth, combined with a high-surface tension mixture, originates sparse crystalline domains where a dendritic morphology is dominant.[39]

The mixing of chloroform or n-hexane with toluene, with a volume ratio of 5:1, makes the jetting of the solution unstable due to their low-boiling points and vapor pressure. However, the use of toluene as the major solvent of the solution makes the jet possible. A clear difference is observed in the morphology of 400×625 µm^2 printed films with the addition of chloroform or n-hexane (Figure S1a, Supporting Information). The lower surface tension of n-hexane enhances evaporation,[40] leading to a film with radial crystalline domains uniformly covering the wettable region.[41] With the addition of chloroform, two distinct morphologies are noticeable: radial crystal domains (spherulites)[42] on the center and elongated crystal on the edge of the wettable region. The use of a single-solvent solution (toluene) instead of a binary-solvent solution (chloroform/toluene) originates larger crystals. This was expected, as a higher boiling point of the solution can be used to slow down the evaporation rate.[43] For this printing system, the above-tested conditions revealed the advantage of using a single solvent over a co-solvent solution to obtain more uniformly printed TIPS-pentacene films.

Aiming to further improve the alignment of elongated crystals with the printing direction, the effects of the concentration and stage temperature were tested. Note that when the stage temperature is increased from 14 to 24 °C, a drastic change in the morphology of the printed films is observed (Figure S1b, Supporting Information). Higher evaporation rates will most likely restrict the migration and reorganization of the molecules during crystallization,[35] leading to a spherulitic pattern instead of plate-like crystals. Interestingly, the variation of the concentration has the least noticeable impact on the morphology of the printed films (Figure S1c, Supporting Information). An increase in concentration from 5 to 14.7 mg mL^{-1} only slightly increases the coverage of the wettable region (400×625 µm^2).[44]

Ultimately, the effect of the geometry of the wettable region on the morphology of the printed films was evaluated. **Figure 3** shows optical images of rectangular TIPS-pentacene printed films of 50×625, 400×625, and 400×1250 µm^2 and the equivalent area of circular and quadrangular geometries. For the smallest dimensions (A = 31 250 µm^2) tested in this

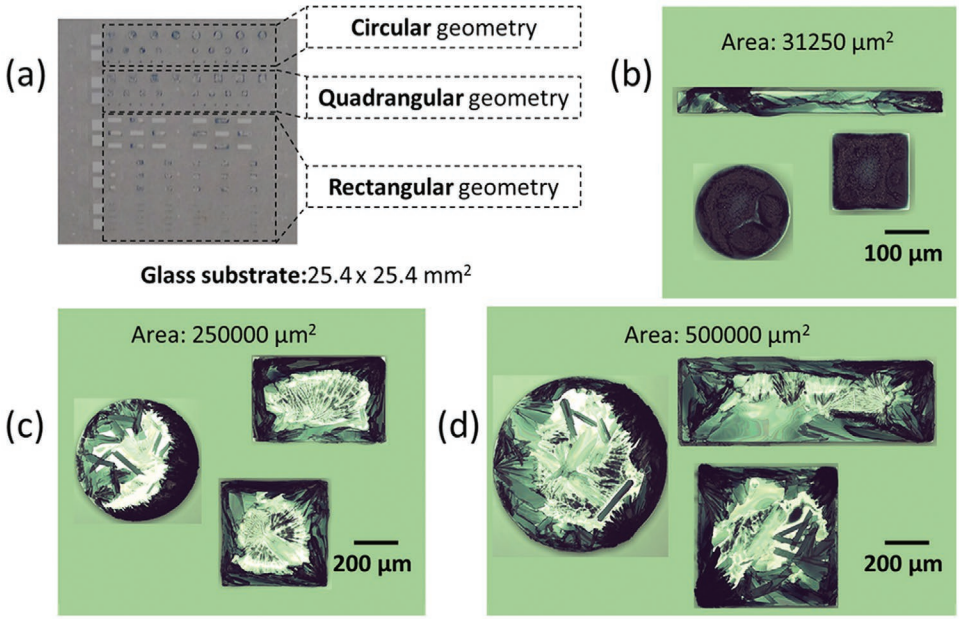

Figure 3. a) Wettability-patterned substrate with TIPS-pentacene printed films and b–d) representative optical images of circular, quadrangular, and rectangular geometries of different equivalent areas.

work, 21 droplets were dispensed with a volume of 123 pL each. To print rectangular films 400 µm-wide and 625 µm-long, 42 spots in line and five droplets per spot were dispensed, with an equivalent total volume of 25.8 nL (210 droplets). To increase the length of the rectangular films, the number of spots was increased to 85 spots, corresponding to a total of 52.2 nL (425 droplets).

In the smallest features, two types of crystal growth occur, platelet and radial domains. The rectangular shape originates plate-like crystals aligned with the printing direction, while in the quadrangular and circular ones, radial crystalline domains are formed.[45] In the latter, as the droplets are dispensed at the center of the features, the concentration gradient is possibly less prominent, thus favoring a more uniform nucleation and radial crystal growth. On the rectangular geometry, where the droplets are dispensed in line, the TIPS-pentacene molecules crystalize along the direction of the concentration gradient.[46]

By increasing feature size, a preferential growth of elongated crystals occurs at the edge rather than at the center, indicating that the wettability contrast of the peripheral region favors crystal nucleation.[47] This implies that the produced Marangoni flow is not enough to overcome the convective flow resulting in low-coverage printed films.[46] Therefore, the solute tends to accumulate at the edge creating a concentration gradient towards the center. Even so, the evaporation rate is low enough for the growing of plate-like crystals, although they have arbitrary orientation.[43]

2.4. Structural Characterization of the Printed Films

The structural properties of the as-prepared printed films can seriously constrain their electrical properties (e.g., response time, dark current, and photogenerated current). As such, a non-destructive and high-resolution characterization tool is needed to infer their crystallinity and the presence of impurities. Micro-Raman spectroscopy allows to assess the structural and chemical quality of a sample by probing vibration modes. Nowadays, micro-Raman spectrometers can perform structural imaging with a lateral resolution of around 1 µm along the micrometer-sized films. The Raman spectra were acquired with a laser source of 633 nm and the laser power was reduced to avoid inducing any thermal damage in the films (P = 1.1 mW). In the visible excitation range, laser-induced fluorescence is an inconvenient characteristic of organic compounds, so the background fluorescence contribution had to be removed from all spectra.[48] As the frequency at which the vibration modes appear depends on the atoms involved and the strength of their bonds, the Raman spectra of rubrene and TIPS-pentacene films were acquired from 551 to 1690 cm^{-1} and from 825 to 1919 cm^{-1}, respectively, to maximize the measured Raman scattering signal.

The rubrene molecule (Figure 1e) consists of a tetracene backbone (four benzene rings) with four substituted phenyl groups. In this work, we have registered and analyzed the 1100–1600 cm^{-1} spectral range where the most intense vibrational modes of rubrene molecules are expected to be observed.[49] To study the Raman vibrational modes along the film presented in **Figure 4**a, seven spectra were acquired along the dotted line (A to G), thus targeting different regions of the film. In this case, the measurements were done without being cautious about exposure to light or ambient conditions. At the positions (A), (B), (E), (F), and (G), the appearance of peaks centered around 1301 and 1313 cm^{-1} (Figure 4c), evidencing the existence of rubrene crystal in the sample.[50] The bands at 1435, 1520, and 1538 cm^{-1} are assigned to the vibrations of the tetracene nuclei of the rubrene molecule[49] and no other spurious phase could be detected within the limit of the technique.

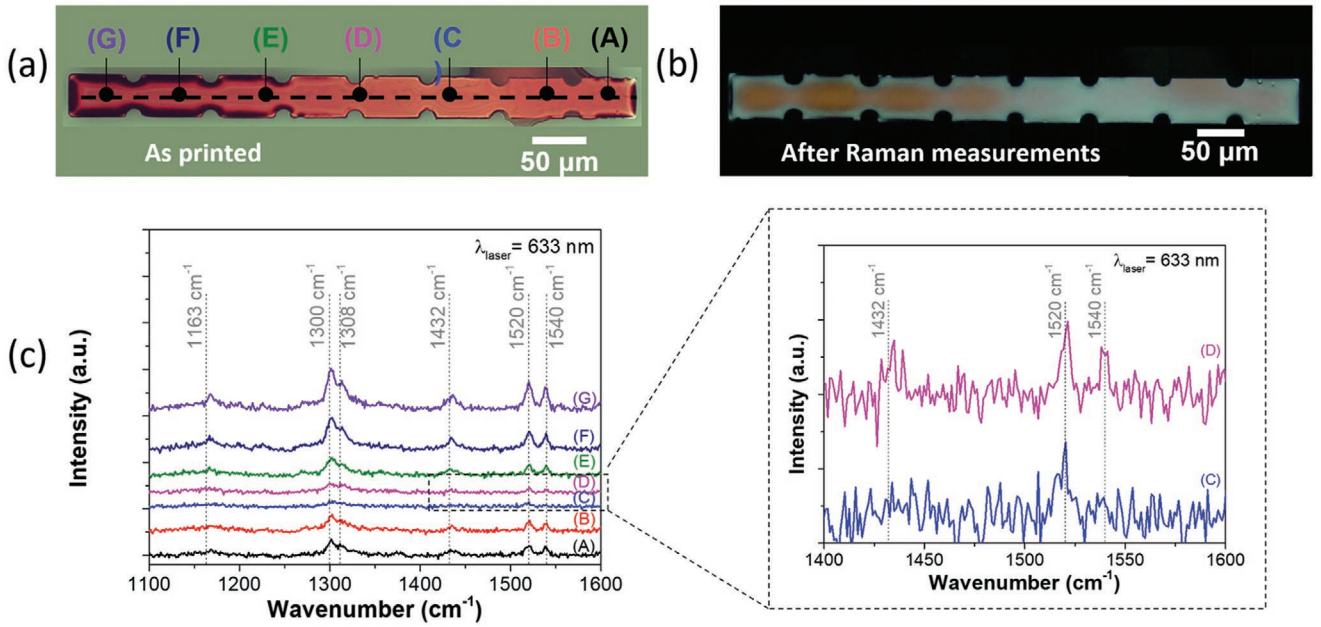

Figure 4. a) Optical image of a rubrene as printed film (50 × 625 µm^2) with seven labeled positions along a dotted line for Raman measurements, b) Optical image of the same printed film after air and light exposure revealing photodegradation, and c) Raman spectra of the positions A to G along the rubrene film, with reference values highlighted in gray.[49]

Note that the intensity of the aforementioned Raman bands at the positions (C) and (D) is much lower when compared to the other spectra, likely due to the film being thinner in this region. However, the relative intensity between the characteristic bands (1301 and 1313 cm^{-1}) is changing, especially at position (C), suggesting a different crystallographic orientation of the rubrene sample. After the Raman measurements, the visual inspection of the film revealed that a discoloration had occurred. The film lost its original dark orange color and became colorless.

To confirm these findings, Raman studies were performed on another rubrene printed film (Figure S2, Supporting Information). This time, the sample was protected from visible light irradiation and the exposure to air was the smallest possible, by keeping the sample under vacuum until its Raman spectrum was recorded (Figure S2a, Supporting Information). The absence of Raman peaks at the positions (X) and (Y) after mapping the sample for 2 h (Figure S2b, Supporting Information) is an indication that a chemical alteration is taking place. This is in line with the change in color from dark orange (pure rubrene) to colorless, observed in both the optical images in Figure 4b and Figure S2, Supporting Information, pointing out rubrene endoperoxide (transparent) formation, which can be explained by the propensity of rubrene films to photo-degradation upon oxygen and light exposure.[51] Nevertheless, in all recorded spectra, the formation of rubrene endoperoxide was not identified, as its peaks were not detected around 1371 and 1604 cm^{-1}, according to Raimondo et al.[52] One possible explanation is the intensity of the signal being too low to be detected. Based on these results, the recorded Raman spectra could be conditioned by the rubrene photo-instability, as the variations in intensity along the film might have a contribution from both thickness and oxidation.

Additionally, the relative intensity ratio of the signature peaks for rubrene was calculated. The table presented in Figure S3, Supporting Information, compares these results with the ones estimated for two orthorhombic rubrene single crystals measured under the same conditions of the printed films. The encountered discrepancies indicate a different crystal orientation of the molecules relative to the substrate. The information about the type of rubrene polymorphs can only be assessed in the low-frequency region of the Raman spectrum (below 300 cm^{-1}),[53] but the signal was too weak to be accounted for Raman imaging.

The other organic compound included in this work, the TIPS-pentacene (Figure 1f), has a pentacene core functionalized with two TIPS groups, increasing its photostability. Usually, when printed, it adopts an edge-on orientation (**Figure 5**a) with respect to the substrate, meaning the pentacene backbone long-axis edge is parallel to the substrate with the molecules packed in a brick-wall motif.[18] To check the crystallinity of the sample, the Raman spectra were recorded at seven different positions (Figure 5b) along a 50 × 625 µm^2 TIPS-pentacene printed film on top of a wettability-patterned substrate and are presented in Figure 5c. The peaks located at 1372 and 1576 cm^{-1} are assigned to the stretching of C—C modes of the short and long axis of the pentacene backbone, respectively.[54] The C—H bending modes from the ends and sides of the pentacene backbone are located at 1156 and 1576 cm^{-1}, respectively. An identical structural fingerprint characterizes all the spectra shown in Figure 5c. Besides the peaks assigned to the pentacene backbone, all other detected peaks are exclusively attributed to the TIPS-pentacene molecule vibrational modes. No significant band shifts are observed in the spectra recorded at different positions and the crystalline nature of the films is confirmed by the narrow peaks.

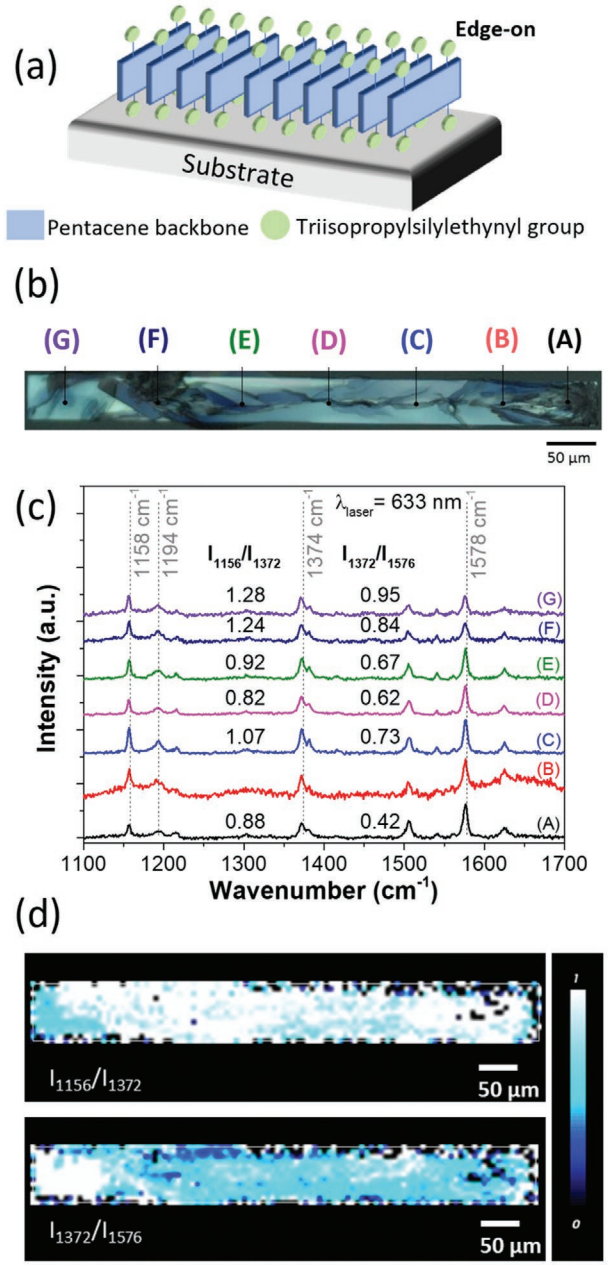

Figure 5. a) Schematics of edge-on molecular packing motifs of TIPS-pentacene, b) Optical image of a TIPS-pentacene rectangular film (50×625 µm^2) with seven labeled positions for Raman measurements, c) the corresponding Raman spectra, with reference values highlighted in gray,[54] and d) 2D Raman maps—the ratios close to 1 are represented in white, while the lowest ratios are represented in dark blue color.

To inspect the films' structural uniformity, an insight into the peak intensity profile of the three most relevant TIPS-pentacene vibrational modes (1158, 1374, and 1578 cm^{-1})[54] is given by the 2D imaging maps along the region of interest (50×625 µm^2) (see Figure S4, Supporting Information), acquired with a grid-line of 6×6 µm^2. The maps share the same color scale to highlight the differences. All three reveal a well-covered surface with TIPS-pentacene molecules but a non-uniform intensity profile. The highest variation is encountered for the intensity map obtained at 1576 cm^{-1}. Additionally, the ratio of intensities of the bands centered at 1156, 1372, and 1576 cm^{-1} were mapped (Figure 5d). The analysis of 2D maps reveals a highly uniform film from the point of view of structural properties, as the relative ratio of intensities is quite similar over a large area (right side of the film). The encountered differences between the left and right parts of the film might indicate distinct molecular orientations or lattice packing deviations.

Xu et al.[55] suggest that the I_{1157}/I_{1374} ratio can be used to monitor the lattice packing variation in solution sheared TIPS-pentacene films. For films highly uniform in thickness, the authors attributed the non-equilibrium packing state (010) to a higher I_{1157}/I_{1374} ratio compared to the equilibrium state (101). Alternatively, D. James et al.[54] proposed a method to determine the in-plane orientation of the pentacene backbone. The authors measured the Raman intensity of the peaks at 1374 and 1578 cm^{-1} as a function of the polarization angle between the laser and the film. From their results, it is clear that mirror-orientated molecules could share the same ratio of intensities between the peaks corresponding to the long and short axis of the pentacene core. Misleading conclusions may be drawn if the relative intensity ratio is used to assess the orientation of the TIPS-pentacene molecules without being complemented with polarized measurements.

From the Raman measurements performed in our work, it is not possible to accurately address the molecular packing and orientation of both rubrene and TIPS-pentacene films. However, it is a simple and non-destructive method to probe inhomogeneities along the film and detect the presence of impurities with the required resolution.

2.5. Application as Photosensing Devices

To validate the use of the wettability-assisted printing method in the optoelectronic industry, both Rubrene and TIPS-pentacene were integrated into planar photosensing devices.

Figure 6a shows a schematic of a micrometric device used to evaluate the photosensitivity of rubrene and TIPS-pentacene printed films. It comprises patterned gold bottom electrodes in a planar configuration with a printed photoactive layer on top. The photoactive area of 50×625 µm^2 was defined using the wettability-assisted process and the optimized printing conditions described above. The current–voltage curves are measured at different light intensities in a two-probe configuration. The applied voltage ranges from −10 to 10 V (for TIPS-pentacene) and −5 to 5 V (for rubrene) (step = 0.5 V), while the current flowing through the photoactive film was measured between the two gold electrodes.

Representative *IV* measurements of rubrene printed film as a function of the electrodes distance (65, 200, 335, and 535 µm) are shown in Figure S5, Supporting Information. The generated current is in the range of the equipment measurement limit (10 pA). Even though the distance between the two probes and the illumination intensity were varied, no significant current variation was detected. This behavior is in line with the formation of rubrene endoperoxide, which is known to reduce conductivity, as reported by Raimondo et al.[52] Different strategies were tested to protect the rubrene solution and the printing

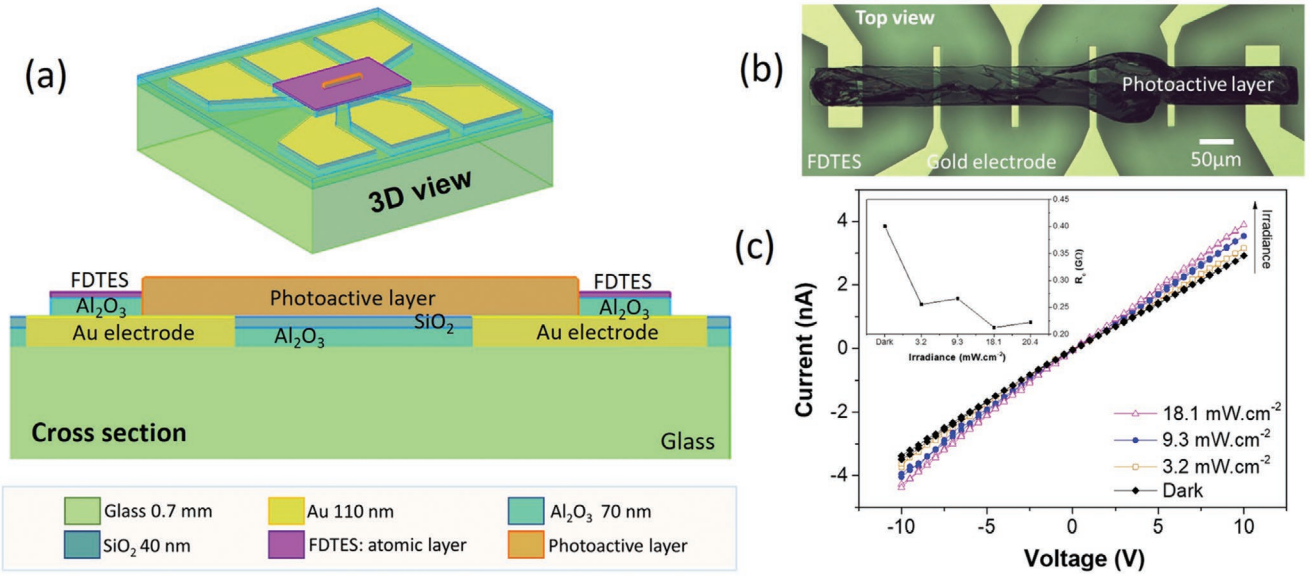

Figure 6. a) Schematic of the photosensing device, b) optical image of a TIPS-pentacene printed film on top of a wettability patterned substrate with gold electrodes underneath, and c) the corresponding *IV* curve of the photosensor under different light intensities.

process from light exposure. However, an oxygen-free atmosphere is not possible with the current instrumental setup used.

The optoelectronic performance of TIPS-pentacene printed film differs hugely from Rubrene when the two electrodes are distanced by 535 µm. Figure 6b shows a TIPS-pentacene printed film on top of gold electrodes. The irregularity in the printed is explained by the formation of secondary droplets, that deviate from the main droplet. As is depicted in Figure 6c, for an applied voltage of 1 V, the measured current is 0.27, 0.26, 0.30, and 0.33 nA, while under dark, exposure to 3.2, 9.3, and 18.1 mW cm^{-2}, respectively. An ohmic behavior without hysteresis is observed, pointing to an adequate matching between the HOMO level of TIPS-pentacene and the work function of gold.[21] The total resistance as a function of light intensity and contact distance is presented in Figure S6, Supporting Information. Under dark, the estimated contact value was 0.40 GΩ, decreasing to 0.21 GΩ when the device was illuminated with 18.1 mW cm^{-2} (inset of Figure 6c). The high contact resistance is most likely to be related to the growth method, misorientation of the organic molecules, or poor contact between the electrodes and the photoactive layer.[56]

Compared to the report of Pipan et al.,[21] our devices show a photocurrent that is about 200 times lower in value. However, they reported a photogenerated current of 60 nA at 1 V, when illuminated with a white LED (P = 19.8 µW), for a TIPS-pentacene inkjet-printed two-terminal photosensing device with interdigitated electrodes, which are known to enhance the photogenerated current. 2D maps of Raman spectra of our printed film (Figure 6b) are included in Figure S7, Supporting Information, discarding the presence of impurities. Nevertheless, these maps also support the evidence of a non-uniform morphology, which may lead to a reduction of the mobility of the charge carriers caused by an arbitrary molecular packing direction. This is consistent with the shape of the $I(t)$ curve (Figure S8, Supporting Information), typical of low-switching photosensing devices. In oligomers, the molecular orientation and packing motif affect the optoelectronic behavior of the device. In the case of planar devices, like phototransistors or photoconductors, it is desirable to have an edge-on orientation with molecules packed perpendicularly to the substrate.[57]

Although rubrene printed films revealed poor electrical performance due to photo-oxidation, when a more stable organic material, such as TIPS-pentacene was tested, the wettability-assisted process presented here could be demonstrated.

3. Conclusion

The combination of non-contact printing with surface energy engineering allows us to confine an organic solution and print crystalline films in targeted locations. Tailor-made designs and shapes of micrometric films of various geometries (quadrangular, circular, and rectangular) of rubrene and TIPS-pentacene were printed to verify the versatility and applicability of the method described here.

The printing conditions were optimized (i.e., number of droplets, spacing between droplets, solvents ratio, and concentration) for the two photoactive materials. The structural properties of the printed structures were mapped with Raman spectroscopy, thus confirming their crystallinity and the absence of incorporated impurities. The detected peaks were only attributed to the vibrational signatures of rubrene (1301 and 1313 cm^{-1}) and TIPS-pentacene (1156, 1372, and 1576 cm^{-1}).

To validate the method, rubrene and TIPS-pentacene were tested as two-terminal photosensors. The formation of rubrene endoperoxide, when the rubrene solution or film is exposed to light and oxygen conditioned its integration into a measurable device. On the contrary, the higher photostability of TIPS-pentacene resulted in an ohmic device, with a generated photocurrent of 0.33 nA under the illumination of 18 mW cm^{-2}.

The method described here could push the present-day technology to provide organic crystalline materials with well-defined

and customizable structures from millimeter to the micrometer range, adequate morphology to prevent charge transport anisotropy, and their seamless integration into functional devices at the wafer level. Compared to vacuum-processing methods, the wettability-assisted process results in lower fabrication costs, provides in situ patterning with high accuracy, and can be adapted to different solution-processing techniques. Furthermore, this strategy could also be applied to other printable materials (organic or inorganic), other types of optoelectronic devices (e.g., phototransistors), and non-rigid substrates.

4. Experimental Section

Materials: Rubrene (97%, Merck), TIPS-pentacene (99%, Merck), acetone (Merck), isopropanol (Merck), toluene (HPLC, 99.9%, Merck), chloroform (HPLC, 99.8%, Merck), n-hexane (97%, Merck), DMF (HPLC, 99.8%, Merck), glass substrates (Eagle XG, Corning), DI water, FDTES (97%, Merck), microstrip (3001, Fujifilm), positive photoresist (PFR7790G27cP, JSR Electronics), and alconox (Merck). All of the above chemicals and solvents were used without further purification.

Contact angle measurements were performed in glass (Corning Eagle XG) coated with 70 nm of SiO_2. A minimum of three droplets of 6 µL of a liquid (DI water, IPA, or toluene) were sequentially dispensed on the surface with a controllable syringe pump (NE 4000, New Era) and 1 mL syringe (CODAN) plus polyethylene tubing BTPE-90 (863.3 µm inner diameter, Instech Lab). The photograph of each droplet was taken and contact angles were estimated through drop shape analysis using the LB-ADSA plugin for ImageJ software.

Wettability-Patterned Substrates: Prior to the fabrication, all the 2.54 × 2.54 cm^2 glass substrates were ultrasonically (T = 60 °C) cleaned using alconox (2 h), followed by isopropanol (30 min), and then dried by compressed air. To define the 400-nm-thick AlSiCu visual guidelines, a 1.4-µm-thick positive photoresist layer was spin-coated onto previously cleaned 2.54 × 2.54 cm^2 glass substrates (2500 rpm for 30 s and baked at 87 °C for 60 s). The photoresist was patterned by optical lithography (Heidelberg Direct Write Laser 2.0 system using a 405 nm laser). After that, the AlSiCu film was deposited by DC magnetron sputtering for 11 s, P = 2 kW, 50 sccm Argon, P_{dep} = 3 mTorr (Nordiko 7000, Nordiko Technical Services Ltd.). After the lift-off step (immersion in microstrip for 2 h in an ultrasonic bath at 60 °C), 200 nm of SiO_2 were deposited by RF magnetron sputtering, P = 140 W, φ_{Ar} = 20 sccm (Alcatel SCM-450). A second lithography was done to protect the target regions from the chemical modification. The substrates were placed upside down inside a desiccator under a vacuum for 48 h and exposed to 20 µL of FDTES. For the PR removal, the substrates were immersed in acetone and placed in an oscillator platform (Tritramax 1000, Heidolph) for 2 min at 600 rpm.

Printing Process: Non-contact printing was carried out using a non-contact printer (GeSiM Nano-Plotter NP2.1) equipped with a piezoelectric activated tip (Nano – Tip A-J Si 02238A). The organic solutions and the buffer solution (toluene) were aspirated from a polypropylene 96-well plate (Greiner bio-one 655291). The printing process was carried out at 21 °C and 50% of humidity. To print the organic solutions, the voltage was set to 50 and 60 V for rubrene and TIPS-pentacene, respectively. The frequency of the jetting was 100 Hz with a pulse width of 80 µs for all the experiments. The droplets were dispensed 0.5 mm above the substrate.

Device Fabrication: For the planar photodetectors, 100 nm of gold and 10 nm of chromium (adhesion layer) were deposited by magnetron sputtering (P = 20 W, φ_{Ar} = 20 sccm, Alcatel SCM-450). Patterns were defined by direct laser photolithography (Heidelberg direct write laser 2.0, diode laser λ = 405 nm) and then transferred to the substrate by ion milling etching (Nordiko 3000) using the following conditions: Ar^+ beam with 29 mA (92 µA cm^{-2}), φ_{Ar} = 8 sccm, acceleration $V+$ = 500 V, extraction $V-$ = 200 V, at 2.4 × 10^{-4} Torr and beam-to-surface angle = 70° for 1200 s. To planarize the metal electrodes, a double oxide layer (70 nm Al_2O_3 + 40 nm SiO_2) was deposited by RF sputtering (P = 200 W, φ_{Ar} = 45 sccm and P = 140 W, φ_{Ar} = 20 sccm, respectively), followed by oxide lift-off. A 70-nm-thick alumina frame (1050 × 1625 μm^2) surrounding the active area (50 × 625 μm^2) was defined by direct-write photolithography and lift-off process. A third photolithography was performed to intentionally modify the alumina frame with FDTES and protect the active area against silanization. The PR was removed by immersing the substrates in acetone and placed them in an oscillator platform (Tritramax 1000, Heidolph) for 2 min at 600 rpm. To fulfil the active area, 21 droplets in line (spacing = 28 µm) of a TIPS-pentacene solution dissolved in toluene (5 mg in 0.34 mL^{-1}) were dispensed (T_{stage} = 19 °C, V = 60 V, f = 100 Hz).

Raman Spectroscopy: High-efficiency confocal Raman inVia Qontor Renishaw spectrometer, where a diffraction grating of 1800 lines/mm and a lens of 50× were used. The excitation laser of a HeNe laser at 633 nm was used at a power of 1.1 mW and a spot size between 1 and 2 µm, with an edge filter down to 100 cm^{-1}. The imaging was performed with an automatized stage with a lateral resolution of 100 nm. The acquisition time was 10 s and 5.5 s for single measurements and mapping, respectively.

Electrical Characterization: *IV* measurements were carried out with a Keithley source meter 2401 in a two-probe configuration. The voltage sweep was applied from –10 to 10 V (step = 0.5 V) and a delay time of 0.05s. The photoactive layer was irradiated using a white LED ring light (Omegon 47405) with variable light intensity. The light intensity was measured with a c-Si photodiode (Thorlabs S120C). The $I(t)$ curves were acquired with the same equipment. The light source was switched from ON (18 mW cm^{-2}) to OFF (dark conditions), while applying a negative voltage bias of 10 V.

Supporting Information

Supporting Information is available from the Wiley Online Library or from the author.

Acknowledgements

The authors acknowledge Fundação para a Ciência e Tecnologia (FCT) for funding UID/05367/2020, PTDC/CTM-NAN/4737/2014, and Network of Extreme Conditions Laboratories (NECL) under NORTE-01-0145-FEDER-22096. S.S. acknowledges financial support through doctoral scholarship SFRH/BD/129827/2017.

Conflict of Interest

The authors declare no conflict of interest.

Data Availability Statement

The data that support the findings of this study are available from the corresponding author upon reasonable request.

Keywords

heterogeneous wettability, micrometric devices, non-contact printing, organic semiconductors, photosensors, surface energy engineering

Received: March 18, 2022
Revised: June 23, 2022
Published online: September 6, 2022

[1] C. Wang, H. Dong, L. Jiang, W. Hu, *Chem. Soc. Rev.* **2018**, *47*, 422.
[2] X. Zhang, H. Dong, W. Hu, *Adv. Mater.* **2018**, *30*, 1801048.

[3] H. Jiang, W. Hu, *Angew. Chem., Int. Ed.* **2020**, *59*, 1408.
[4] X. Huang, D. Ji, H. Fuchs, W. Hu, T. Li, *ChemPhotoChem* **2020**, *4*, 9.
[5] G. Schweicher, G. Garbay, R. Jouclas, F. Vibert, F. Devaux, Y. H. Geerts, *Adv. Mater.* **2020**, *32*, 1905909.
[6] C. Wang, P. Gu, B. Hu, Q. Zhang, *J. Mater. Chem. C* **2015**, *3*, 10055.
[7] Y. Li, Q. Qian, X. Zhu, Y. Li, M. Zhang, J. Li, C. Ma, H. Li, J. Lu, Q. Zhang, *InfoMat* **2020**, *2*, 995.
[8] J. Lian, Z. Vatansever, M. Noshad, M. Brandt-Pearce, *J. Phys. Photonics* **2019**, *1*, 012001.
[9] G. A. Mapunda, R. Ramogomana, L. Marata, B. Basutli, A. S. Khan, J. M. Chuma, *Wirel. Commun. Mob. Comput.* **2020**, *2020*, 8881305.
[10] J. Oliveira, R. Brito-Pereira, B. F. Gonçalves, I. Etxebarria, S. Lanceros-Mendez, *Org. Electron.* **2019**, *66*, 216.
[11] S. Chung, K. Cho, T. Lee, *Adv. Sci.* **2019**, *6*, 1801445.
[12] K. Yan, J. Li, L. Pan, Y. Shi, *APL Mater.* **2020**, *8*, 120705.
[13] C. Liu, H. Zhou, Q. Wu, F. Dai, T. K. Lau, X. Lu, T. Yang, Z. Wang, X. Liu, C. Liu, *ACS Appl. Mater. Interfaces* **2018**, *10*, 39921.
[14] G. Hu, L. Yang, Z. Yang, Y. Wang, X. Jin, J. Dai, Q. Wu, S. Liu, X. Zhu, X. Wang, T. C. Wu, R. C. T. Howe, T. Albrow-Owen, L. W. T. Ng, Q. Yang, L. G. Occhipinti, R. I. Woodward, E. J. R. Kelleher, Z. Sun, X. Huang, M. Zhang, C. D. Bain, T. Hasan, *Sci. Adv.* **2020**, *6*, eaba5029.
[15] J. Sun, B. Bao, M. He, H. Zhou, Y. Song, *ACS Appl. Mater. Interfaces* **2015**, *7*, 28086.
[16] B. B. Patel, Y. Diao, *Nanotechnology* **2018**, *29*, 044004.
[17] Y. Diao, L. Shaw, Z. Bao, S. C. B. Mannsfeld, *Energy Environ. Sci.* **2014**, *7*, 2145.
[18] P. Yu, Y. Zhen, H. Dong, W. Hu, *Chem* **2019**, *5*, 2814.
[19] X. Zhang, W. Deng, R. Jia, X. Zhang, J. Jie, *Small* **2019**, *15*, 1900332.
[20] J. Serra, S. Sequeira, I. Domingos, A. Paracana, E. Maçôas, L. V. Melo, B. J. Pires, S. Cardoso, D. C. Leitao, H. Alves, *Adv. Funct. Mater.* **2021**, *31*, 2105638.
[21] G. Pipan, M. Bogar, A. Ciavatti, L. Basiricò, T. Cramer, B. Fraboni, A. Fraleoni-Morgera, *Adv. Mater. Interfaces* **2018**, *5*, 1700925.
[22] H. Minemawari, T. Yamada, H. Matsui, J. Tsutsumi, S. Haas, R. Chiba, R. Kumai, T. Hasegawa, *Nature* **2011**, *475*, 364.
[23] D. Janssen, R. De Palma, S. Verlaak, P. Heremans, W. Dehaen, *Thin Solid Films* **2006**, *515*, 1433.
[24] L. Wang, U. S. Schubert, S. Hoeppener, *Chem. Soc. Rev.* **2021**, *50*, 6507.
[25] Y. Yang, A. M. Bittner, S. Baldelli, K. Kern, *Thin Solid Films* **2008**, *516*, 3948.
[26] C. G. Allen, D. J. Baker, J. M. Albin, H. E. Oertli, D. T. Gillaspie, D. C. Olson, T. E. Furtak, R. T. Collins, *Langmuir* **2008**, *24*, 13393.
[27] A. Chandekar, S. K. Sengupta, J. E. Whitten, *Appl. Surf. Sci.* **2010**, *256*, 2742.
[28] B. Bhushan, D. Hansford, K. K. Lee, *J. Vac. Sci. Technol.* **2006**, *24*, 1197.
[29] S. Schlisske, M. Held, T. Rödlmeier, S. Menghi, K. Fuchs, M. Ruscello, A. J. Morfa, U. Lemmer, G. Hernandez-sosa, *Langmuir* **2018**, *34*, 5964.
[30] Z. Zhan, J. An, Y. Wei, V. T. Tran, H. Du, *Nanoscale* **2017**, *9*, 965.
[31] A. M. Gaikwad, Y. Khan, A. E. Ostfeld, S. Pandya, S. Abraham, A. C. Arias, *Org. Electron.* **2016**, *30*, 18.
[32] G.-H. Lim, J.-M. Zhuo, L.-Y. Wong, S.-J. Chua, L.-L. Chua, P. K. H. Ho, *Org. Electron.* **2014**, *15*, 449.
[33] T. Matsukawa, Y. Takahashi, T. Tokiyama, K. Sasai, Y. Murai, N. Hirota, Y. Tominari, N. Mino, M. Yoshimura, M. Abe, J. Takeya, Y. Kitaoka, Y. Mori, S. Morita, T. Sasaki, *Jpn. J. Appl. Phys.* **2008**, *47*, 8950.
[34] K. Sim, H. Na, J. Park, J. Lee, J. Do, S. Pyo, *Org. Electron.* **2018**, *56*, 76.
[35] P. He, B. Derby, *Adv. Mater. Interfaces* **2017**, *4*, 1700944.
[36] S. Y. Cho, J. M. Ko, J. Lim, J. Y. Lee, C. Lee, *J. Mater. Chem. C* **2013**, *1*, 914.
[37] K. N. Choi, K. S. Kim, K. S. Chung, H. Lee, *IEEE Trans. Device Mater. Reliab.* **2009**, *9*, 489.
[38] G. P. Rigas, M. M. Payne, J. E. Anthony, P. N. Horton, F. A. Castro, M. Shkunov, *Nat. Commun.* **2016**, *7*, 13531.
[39] Z. He, Z. Zhang, K. Asare-Yeboah, S. Bi, J. Chen, D. Li, *Polymers* **2021**, *13*, 402.
[40] L. Chou, W. Chang, G. He, Y. Chiu, C. Liu, *React. Funct. Polym.* **2016**, *108*, 130.
[41] S. Wang, X. Zhao, Y. Tong, Q. Tang, Y. Liu, *Adv. Mater. Interfaces* **2020**, *7*, 1901950.
[42] H. Yoo, H. H. Choi, T. J. Shin, T. Rim, K. Cho, S. Jung, J.-J. Kim, *Adv. Funct. Mater.* **2015**, *25*, 3658.
[43] Z. He, J. Chen, D. Li, *J. Vac. Sci. Technol.* **2019**, *37*, 040801.
[44] D. L. Kabir, I. Mejia, M. R. Perez, J. C. Ramos-Hernandez, M. A. Quevedo-Lopez, *J. Electron. Mater.* **2015**, *44*, 490.
[45] Y. Jo, H. Park, H. Ahn, Y. H. Kim, S. Jung, *Flex. Print. Electron.* **2019**, *4*, 042001.
[46] H. Zhao, Z. Wang, G. Dong, L. Duan, *Phys. Chem. Chem. Phys.* **2015**, *17*, 6274.
[47] Y.-H. Kim, B. Yoo, J. E. Anthony, S. K. Park, *Adv. Mater.* **2012**, *24*, 497.
[48] P. Finnie, J. Ouyang, J. Lefebvre, *Sci. Rep.* **2020**, *10*, 9172.
[49] J. W. Wolf, *Optical Characterization of Organic Single Crystals*, PhD thesis, Chapel Hill, **2006**.
[50] M. Kadlečíková, J. Breza, J. Liday, H. Sitter, S. A. Al-Baqi, *J. Electr. Eng.* **2010**, *61*, 296.
[51] W. R. Mateker, T. Heumueller, R. Cheacharoen, I. T. Sachs-Quintana, M. D. McGehee, J. Warnan, P. M. Beaujuge, X. Liu, G. C. Bazan, *Chem. Mater.* **2015**, *27*, 6345.
[52] L. Raimondo, S. Trabattoni, M. Moret, N. Masciocchi, M. Masino, A. Sassella, *Adv. Mater. Interfaces* **2017**, *4*, 1700670.
[53] J. Socci, T. Salzillo, R. G. D. Valle, E. Venuti, A. Brillante, *Solid State Sci.* **2017**, *71*, 146.
[54] D. T. James, B. K. C. Kjellander, W. T. T. Smaal, G. H. Gelinck, C. Combe, I. McCulloch, R. Wilson, J. H. Burroughes, D. D. C. Bradley, J. S. Kim, *ACS Nano* **2011**, *5*, 9824.
[55] J. Xu, Y. Diao, D. Zhou, Y. Mao, G. Giri, W. Chen, N. Liu, S. C. B. Mannsfeld, G. Xue, Z. Bao, *J. Mater. Chem. C* **2014**, *2*, 2985.
[56] Y.-J. Lee, Y. U. Lee, H. Yeon, H. Shin, L. A. Evans, Y.-C. Joo, *Appl. Phys. Lett.* **2013**, *103*, 241904.
[57] A. M. Hiszpanski, Y.-L. Loo, *Energy Environ. Sci.* **2014**, *7*, 592.